The Seismic Record
A journal of the Seismological Society of America

Coseismic Slip Model of the 19 September 2022 M_w 7.6 Michoacán, Mexico, Earthquake: A Quasi-Repeat of the 1973 M_w 7.6 Rupture

Chengli Liu[*1], Thorne Lay[2], Yefei Bai[3,4], Ping He[1], and Xiong Xiong[1]

Abstract

On 19 September 2022, a major earthquake struck the northwestern Michoacán segment along the Mexican subduction zone. A slip model is obtained that satisfactorily explains geodetic, teleseismic, and tsunami observations of the 2022 event. The preferred model has a compact large-slip patch that extends up-dip and northwestward from the hypocenter and directly overlaps a 1973 M_w 7.6 rupture. Slip is concentrated offshore and below the coast at depths from 10 to 30 km with a peak value of ~2.9 m, and there is no detected coseismic slip near the trench. The total seismic moment is 3.1×10^{20} N · m (M_w 7.6), 72% of which is concentrated in the first 30 s. Most aftershocks are distributed in an up-dip area of the mainshock that has small coseismic slip, suggesting near-complete strain release in the large-slip patch. Teleseismic *P* waveforms of the 2022 and 1973 earthquakes are similar in duration and complexity with high cross-correlation coefficients of 0.68–0.98 for long *P* to *PP* signal time windows, indicating that the 2022 earthquake is a quasi-repeat of the 1973 earthquake, possibly indicating persistent frictional properties. Both the events produced more complex *P* waveforms than comparable size events along Guerrero and Oaxaca, reflecting differences in patchy locking of the Mexican megathrust.

Cite this article as Liu, C., T. Lay, Y. Bai, P. He, and X. Xiong (2023). Coseismic Slip Model of the 19 September 2022 M_w 7.6 Michoacán, Mexico, Earthquake: A Quasi-Repeat of the 1973 M_w 7.6 Rupture, *The Seismic Record*. **3**(**2**), 57–68, doi: 10.1785/0320220042.

Introduction

Tectonic strain accumulation along the Mexican subduction zone is produced by the Rivera and Cocos plates underthrusting the North American plate at from 2.5 to 7.0 cm/yr (DeMets *et al.*, 2010). This strain is released by various seismic or aseismic processes, including large earthquakes, slow slip events, and tectonic tremors (Astiz *et al.*, 1987; Franco *et al.*, 2005; Ramírez-Herrera *et al.*, 2010; Graham *et al.*, 2014; Brudzinski *et al.*, 2016; Cruz-Atienza *et al.*, 2021). The Jalisco–Colima–Michoacán region, located in the northwestern Mexican subduction zone, involves all the three plates (Fig. 1). Prior to 2022, this region experienced multiple large damaging earthquakes (Singh *et al.*, 1981; Astiz *et al.*, 1987; Cosenza-Muralles *et al.*, 2022). These include the 3 June 1932 (M_s 8.2) Jalisco earthquake, which is the largest instrumentally recorded earthquake along the Mexican subduction zone (Singh *et al.*, 1985); the Colima–Jalisco megathrust earthquake of 9 October 1995 (M_w 8.0) (Mendoza and Hartzell, 1997; Ortiz *et al.*, 1998); a megathrust rupture on 30 January 1973 (M_w 7.6) (Reyes *et al.*, 1979; Santoyo *et al.*, 2006); the great earthquake on 19 September 1985 (M_w 8.1), which ruptured the previously recognized Michoacán seismic gap (UNAM Seismology Group, 1986; Mendoza and Hartzell, 1989); and the Tecomán earthquake of 22 January 2003

1. School of Geophysics and Geomatics, China University of Geosciences, Wuhan, Hubei, China, https://orcid.org/0000-0001-5643-3428 (CL); https://orcid.org/0000-0001-7691-8350 (PH); https://orcid.org/0000-0002-7248-6308 (XX); 2. Department of Earth and Planetary Sciences, University of California Santa Cruz, Santa Cruz, California, U.S.A., https://orcid.org/0000-0003-2360-4213 (TL); 3. Ocean College, Zhejiang University, Zhoushan, Zhejiang, China, https://orcid.org/0000-0003-3323-3348 (YB); 4. Hainan Institute, Zhejiang University, Sanya, Hainan, China

*Corresponding author: liuchengli@cug.edu.cn

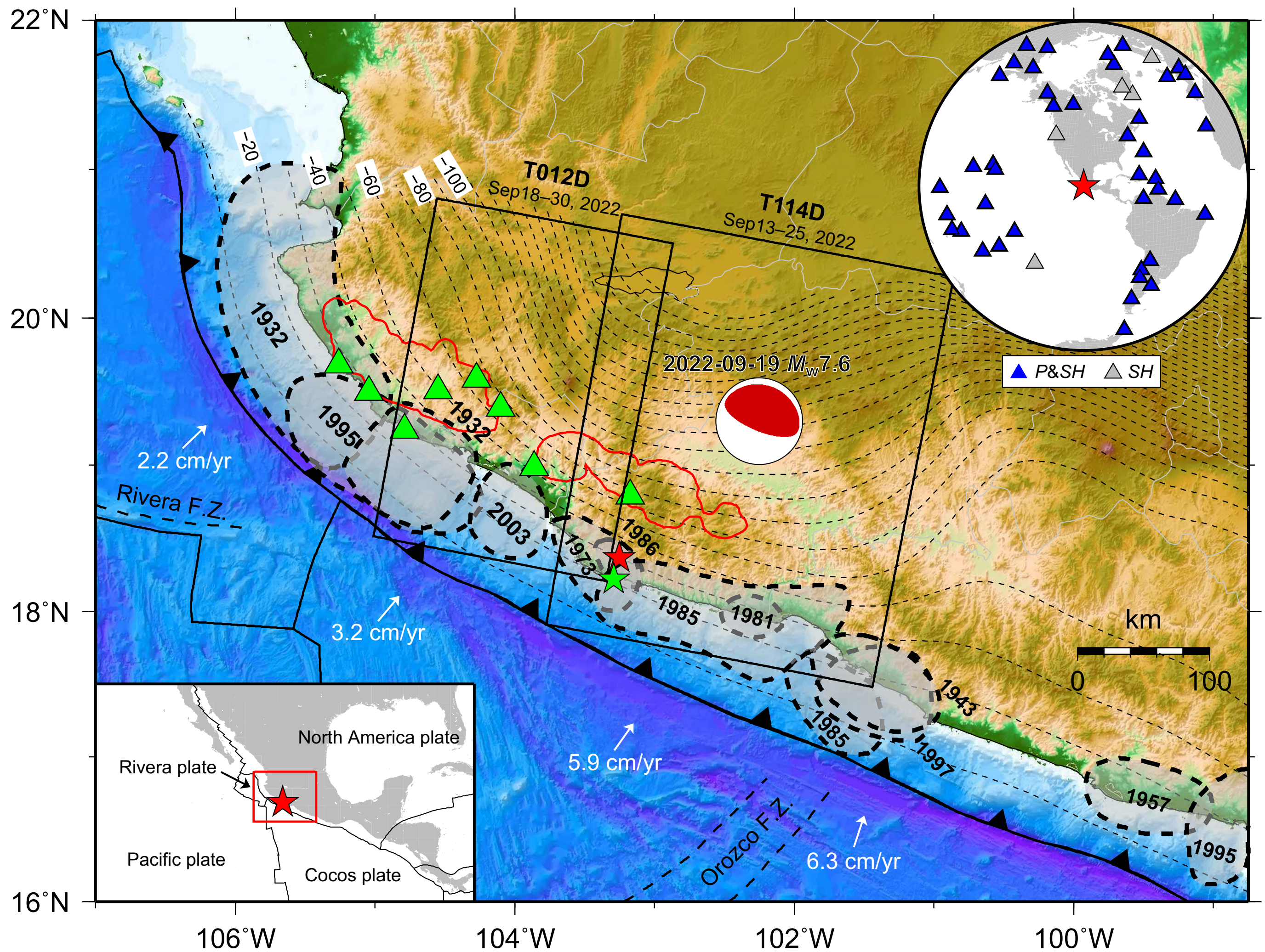

(M_w 7.6) (Yagi *et al.*, 2004; Gómez-González *et al.*, 2010; Martínez López and Mendoza, 2018), which partly filled a gap between the 1995 and 1973 events in the Jalisco–Colima region. A smaller M_w 7.0 thrust event struck within the 1973 rupture zone on 30 April 1986 (Fig. 1), but the amplitudes are a factor of 3–4 lower than for the 1973 event, so we do not consider the 1986 event further here. Interseismic fault locking along the 1973 rupture was inferred to be low (<0.3 along the coast and just offshore) (Cosenza-Muralles *et al.*, 2022), but there is a paucity of Global Positioning System (GPS) sites along Michoacan, so this is not well resolved, and inferences of high locking near the trench are based on assumptions not resolved by data.

On 19 September 2022, the Michoacán region was struck again by a major earthquake (18:05:08 UTC, 18.455° N

Figure 1. Tectonic setting of the northwestern section of the Mexico subduction zone. Gray transparent areas outlined by thick, black dashed lines are the approximate source areas of large historical events. The black barbed curve marks the plate boundary between the Rivera or Cocos and North American plates. The white arrow indicates the convergence rate from the MORVEL 2010 model (DeMets *et al.*, 2010). The black dashed lines outline the Orozco and Rivera fracture zones (Singh and Mortera, 1991). Thin black dashed lines with a 20 km interval show the depth contours of the Slab2 model (Hayes *et al.*, 2018). The red contours indicate areas of tectonic tremor (Brudzinski *et al.*, 2016). The red focal mechanism and star are the U.S. Geological Survey National Earthquake Information Center (USGS-NEIC) epicenter and *W*-phase solution or the 2022 event, respectively, and the green star is the Servicio Sismológico Nacional (SSN) epicenter. The 1986 event was much smaller (M_w 7.0), and may overlap portions of the 1973 and 2022 events. Green triangles denote GNSS sites, and solid black rectangles represent the footprints and time intervals of two descending Sentinel-1 images used in the joint inversion. The upper inset shows the locations of teleseismic stations providing *P* and *SH* recordings used in the joint inversion.

102.956° W, 26.9 km depth, U.S. Geological Survey National Earthquake Information Center [USGS-NEIC]). The USGS-NEIC W-phase solution indicates a predominantly shallowly dipping thrust mechanism with strike $\phi = 287°$, dip $\delta = 18°$, and rake $\lambda = 86°$. The seismic moment $M_0 = 2.674 \times 10^{20}$ N · m (M_w 7.6), and the centroid depth is 23.5 km. Mexico's Servicio Sismológico Nacional (SSN) reports the mainshock epicenter as 18.22° N and 103.29° W at a depth of 15 km, with a moment tensor solution given by $\phi = 306.1°$, $\delta = 9.1°$, and $\lambda = 114°$. The $M_0 = 4.47 \times 10^{20}$ N · m (M_w 7.7), and the centroid depth is 11.5 km, with the shallower dip accounting for the significant seismic moment difference from the USGS-NEIC solution. The Global Centroid Moment Tensor (Global CMT) solution is intermediate and has $\phi = 303°$, $\delta = 12°$, and $\lambda = 102°$ with a centroid depth of 18.6 km, and $M_0 = 3.83 \times 10^{20}$ N · m (M_w 7.7). This event is close to the comparable size 1973 event (Fig. 1) and a prior M_w 7.6 event on 15 April 1941 (Singh *et al.*, 1981; Astiz *et al.*, 1987). It is unclear whether this region ruptured in either of the two comparable magnitudes events in 1911, located to the northwest and southeast (Singh *et al.*, 1981).

As a result of the relatively short average recurrence interval (30–50 yr) for many portions of the Mexican subduction zone (Singh *et al.*, 1981), an increasing number of recent large earthquakes have ruptured regions in close proximity to prior seismically recorded large events, some of which have been analyzed for space–time slip distributions (Martínez López and Mendoza, 2018; Dominguez *et al.*, 2022; Iglesias *et al.*, 2022; Yan *et al.*, 2022). These recurrent ruptures provide valuable information about the possible persistence of asperities and frictional behavior over multiple seismic cycles. The 2022 Michoacán earthquake was located in the rupture area of the 1973 event with a similar magnitude, and both the events were recorded by teleseismic digital seismic recordings, which presents the opportunity to obtain insight into the frictional properties of the Michoacán region. To evaluate this, we jointly invert teleseismic body waves, high-rate Global Navigation Satellite System (GNSS) waveforms, GNSS static offsets, and Interferometric Synthetic Aperture Radar (InSAR) data to constrain the rupture evolution and overall distribution of coseismic slip for the 2022 event. Forward modeling of observed tsunami waveforms and analysis of the long-period surface-wave source spectra are used to validate the slip model. Then, we compare colocated seismograms of the 2022 and 1973 events to evaluate rupture similarity and to assess whether the two events involve repeated failure of a persistent asperity.

Data and Method

Teleseismic data

High signal-to-noise ratio teleseismic broadband seismic recordings within an epicentral distance range of 30°–90° were obtained from the Incorporated Research Institutions for Seismology Data Management Center, providing well-distributed azimuthal coverage (Fig. 1). The instrument responses were deconvolved to obtain ground velocities for P waves and displacements for SH waves. We cut the time series to a 100 s duration from the first arrivals, and applied resampling to 0.2 s and a bandpass filter of 0.033–1 Hz for each seismogram, and then precisely align P- and SH-wave first arrival onsets manually (Liu *et al.*, 2019).

Geodetic data

We processed 1 s sample rate GNSS data from the University Navstar Consortium (UNAVCO) for eight stations close to the source (Figs. 1 and 2a) using the Canadian Spatial Reference System precise point positioning online web service. The horizontal components have higher signal-to-noise ratios, whereas the vertical components are noisier. To reduce the high-frequency noise, a lowpass filter with a 0.5 Hz corner was applied to the observations (Fig. 2b). We also obtained coseismic static displacements for 11 GNSS sites (Fig. 2a) from the Network of the Americas operated by UNAVCO and processed by the Geodesy Laboratory at Central Washington University.

Two pairs of C-band Sentinel-1 satellite synthetic aperture radar (SAR) images with complete coverage were selected to derive the coseismic displacements for the 2022 event, including two descending orbit pairs (T012D and T114D; Fig. 1). We processed these SAR data using the commercial GAMMA software (Wegnüller *et al.*, 2016). The 1 arcsec the shuttle radar topography mission (SRTM) digital elevation model (DEM) (Farr *et al.*, 2007) was adapted to minimize the topography-contributed InSAR phase and to reduce stratified atmospheric artifacts related to regional topography. InSAR observations show apparent deformation associated with this earthquake in the line-of-sight (LOS) direction (Fig. 2d). Then, we applied a standard quadtree method to downsample the two interferograms, and obtained 691 and 597 points for T012D and T114D for the following joint inversion.

Tsunami data

We use tsunami observations from five tide gauge stations and one ocean-bottom pressure sensor from station 43412 of the Deep-Ocean Assessment and Reporting of Tsunamis (DART) network (Fig. 3a). Ten-hour-long water-level records with

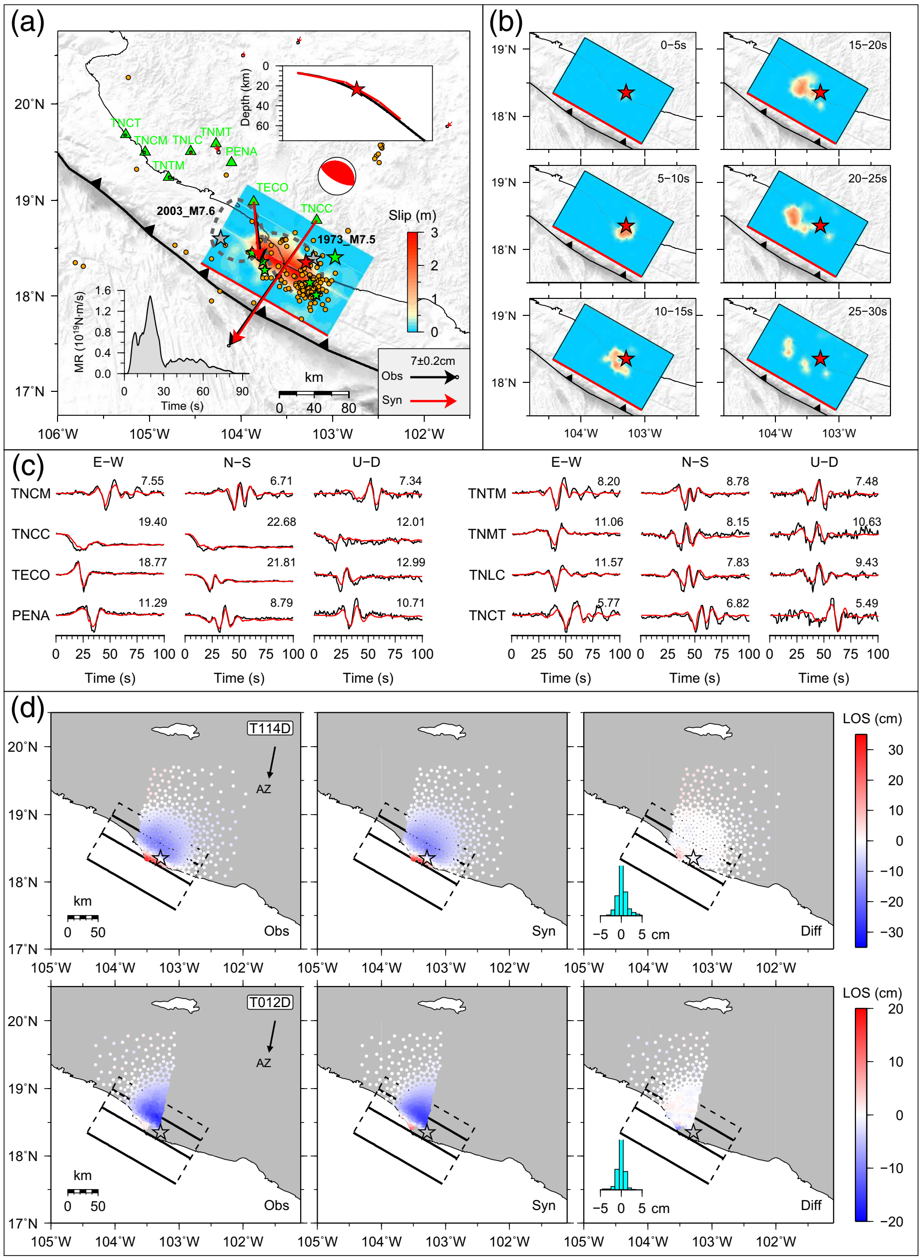

Figure 2. (a) Map view of the preferred slip model of the 2022 mainshock, superimposed with magnitude ≥4.0 aftershocks from the SSN catalog within two months of the mainshock. The red star and focal mechanism indicate the preferred epicenter and average Centroid Moment Tensor (CMT) solution from the preferred slip model. The gray stars and dashed contours are the epicenters and approximate source areas of the 1973 and 2003 events, respectively. The green stars indicate the aftershocks with magnitude ≥5.0 from the SSN catalog. The vectors show comparisons between observed (black) and computed (red) horizontal GNSS statics. The lower left inset is the moment rate function. The upper right inset shows a cross section of the model geometry, and the red lines indicate the position of the fault segments, and the black line indicates the plate interface from the Slab2 model (Hayes *et al.*, 2018). The green triangles are the locations of high-rate GNSS stations. (b) Map view of slip evolution in 5 s time windows. (c) Comparisons of high-rate GNSS displacement time series (black) and synthetic seismograms (red). Station names are indicated on the left, and peak values are shown on the upper right in cm. The waveform misfit value is 0.224, as defined by Ji *et al.* (2002). (d) Interferometric Synthetic Aperture Radar line-of-sight displacement image for two descending tracks (left column) with model predictions (middle column) and differences (right column). The warmer colors (positive) show movement toward the satellite, and cooler colors (negative) show movement away from the satellite. The rectangles represent the fault segments, and the histograms show the distribution of the fitting errors. The black arrows indicate the azimuth (AZ) direction of each track.

1 min temporal resolution at tide gauge stations Puerto Vallarta, Manzanillo, Lazaro, Zihuatanejo, and Acapulco along Mexico coast were retrieved from the web service provided by the UNESCO sea-level station monitoring facility. Missing time slots in the five records are filled at 1 min intervals, and absent measurements are estimated through spline interpolation. The resultant continuous time series were then high-pass filtered to remove tidal fluctuation, and truncated front and back, yielding 6 hr records starting from the earthquake initiation time. Similar procedures were also applied to the record of DART 43412, giving a de-tided time series with 6 hr and 1 min intervals for comparison with the model output.

Finite-fault modeling strategy

To account for the varying dip along the subducting plate interface (Abbott and Brudzinski, 2015; Hayes *et al.*, 2018), we model the fault plane with three contiguous rectangular planar segments with strike (300°) and depth-varying dip angles (11°, 30°, and 37°; Fig. 2a) that conform well with the Slab2 model (Hayes *et al.*, 2018). These segments are divided into 204 10 × 10 km subfaults. We invert the kinematic slip distribution of the 2022 Michoacán earthquake using a nonlinear inversion method (Ji *et al.*, 2002, 2003) that solves for slip, rake, rupture time, and rise time of each subfault simultaneously. A simulated annealing algorithm solves for these parameters within wide prescribed ranges. The rake angles of subfaults can vary from 57° to 117°, and the slip amplitudes range from 0 to 3 m. The rise time and fall time of the asymmetric subfault slip rate functions range from 0.6 to 6 s. Therefore, the subfault source time function durations are bounded between 1.2 and 12 s. A series of preliminary inversions evaluate the rapid epicenter locations reported by NEIC and SSN, searching for the optimal hypocenter for our data distribution. This results in the rupture initiating with hypocenter 18.351° N, 103.29° W, at a depth of 23.7 km. Kinematic and static Green's functions are calculated using a 1D layered velocity structure (Yagi *et al.*, 2004), with the distinct data types in the inversion weighted equally, based on frequency contents and balancing of the signal power in the respective datasets.

Results

Finite-fault model

The preferred slip model of the 2022 Michoacán earthquake from the joint inversion of seismic and geodetic data is shown in Figure 2a. It has $M_0 = 3.1 \times 10^{20}$ N · m (M_w 7.6), and a slip centroid depth of 22.2 km, which is deeper than the Global CMT centroid (18.6 km) and comparable with the USGS-NEIC *W*-phase centroid estimate (23.5 km). The preferred model has an elongated slip patch extending ~80 km along strike, located between 10 and 30 km depth, with a peak slip of ~2.9 m, and without significant shallow rupture (Fig. 2a). We test the stability of the results by perturbing the strike of the fault and the precise dips of the segments, and find that the slip pattern is very stable. Figure 2b shows the spatiotemporal evolution of slip for time increments of 5 s, revealing a unilateral complex rupture process. The total duration of the rupture is about 80 s (Fig. 2a), with 48% of the total moment concentrated in the first 30 s, mainly corresponding to the middle fault segment (Fig. 2b). About 47% of the moment is from rupture of the shallower fault segment and 5% on the deeper fault segment. The radiated scaled energy moment value estimated from broadband radiated elastic energy in the far field ($E_r = 2.7 \times 10^{15}$ J; Convers and Newman, 2011) and seismic moment (M_0) from our joint inversion is 0.87×10^{-5}, slightly lower relative to other interplate thrust events (1.06×10^{-5}; Ye *et al.*, 2016).

The preferred slip model fits the GNSS static offsets and high-rate displacement waveforms well (Fig. 2a,c), and the root-mean-square (rms) value of static GPS is 0.26 cm. The predicted InSAR LOS displacements and the misfit residuals are shown in Figure 2d. The rms of residuals are 1.3 cm (track T114D) and 1.2 cm (track T012D). Synthetic teleseismic body waves generally show a reasonable-to-good fit to the observations for *P*-wave ground velocities (Fig. 4a) and *SH* displacements (Fig. 4b), and the model accounts for the large amplitude, longer period body-wave phases of the records well; however, high-frequency *P*-wave motions are less well modeled, probably due to the limited resolution of the 1D crustal velocity model that we use.

Model validation

The inverted finite-fault model is tested using forward modeling of long-period surface-wave spectra and tsunami recordings.

Measured spectral amplitudes for Rayleigh waves (Fig. 4c) and Loves waves (Fig. 4d) at a period of $T = 227.56$ s are compared with point-source calculations for velocity model Preliminary Reference Earth Model (PREM) for the best double couples of the USGS-NEIC *W*-phase moment tensor, the Global CMT, and our composite three-segment finite-fault model. The spectral method follows the work of Kanamori and Given (1981). These comparisons, as well as those for other periods, indicate that the finite-fault model fits the

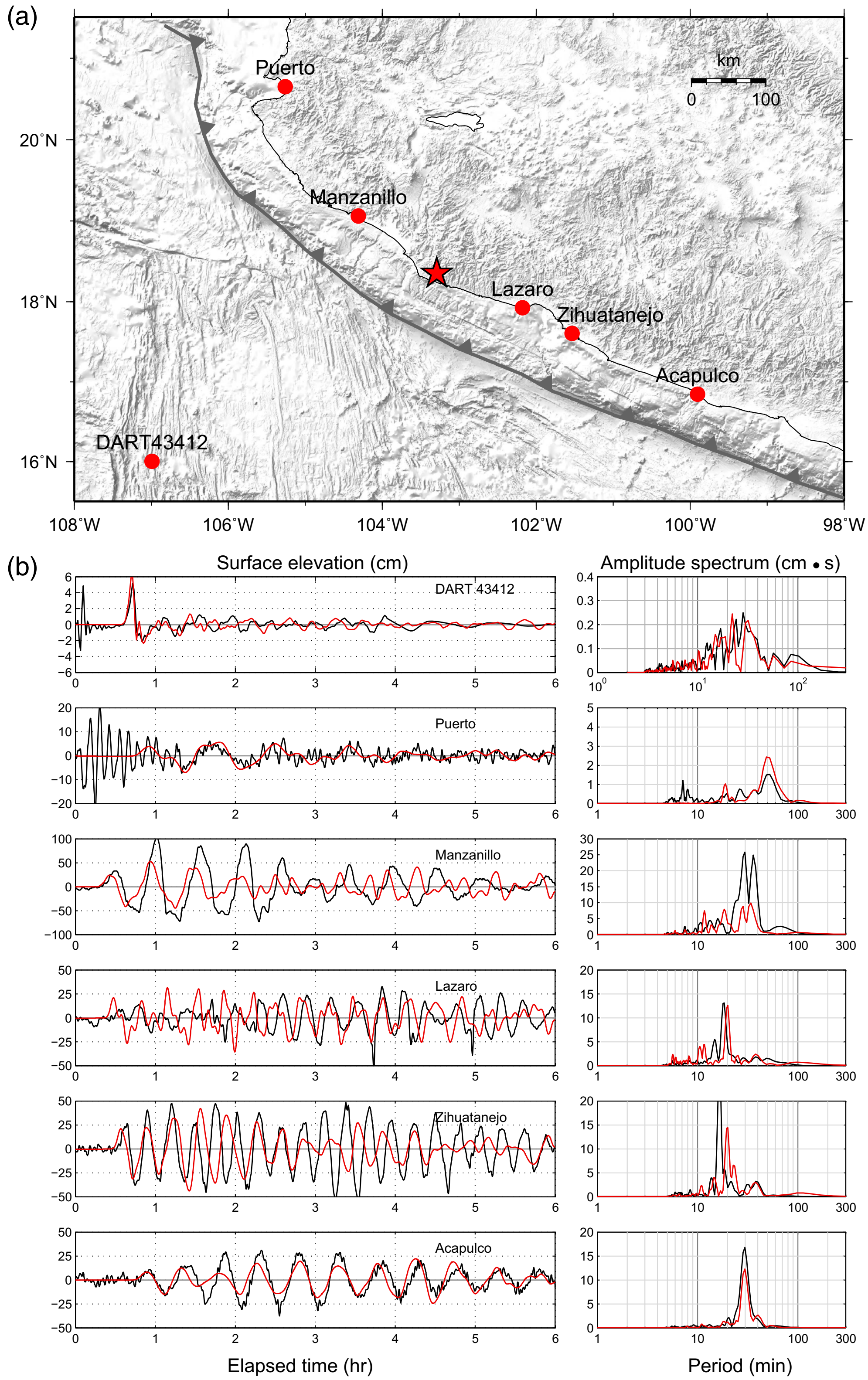

Figure 3. (a) Distribution of Deep-Ocean Assessment and Reporting of Tsunamis (DART) and tide gauge stations providing tsunami recordings (red dots). The red star shows the hypocenter of the 2020 earthquake. (b) Comparisons between the recorded (black) and modeled (red) waveforms and spectra at DART and tide gauges stations are shown in panel (a).

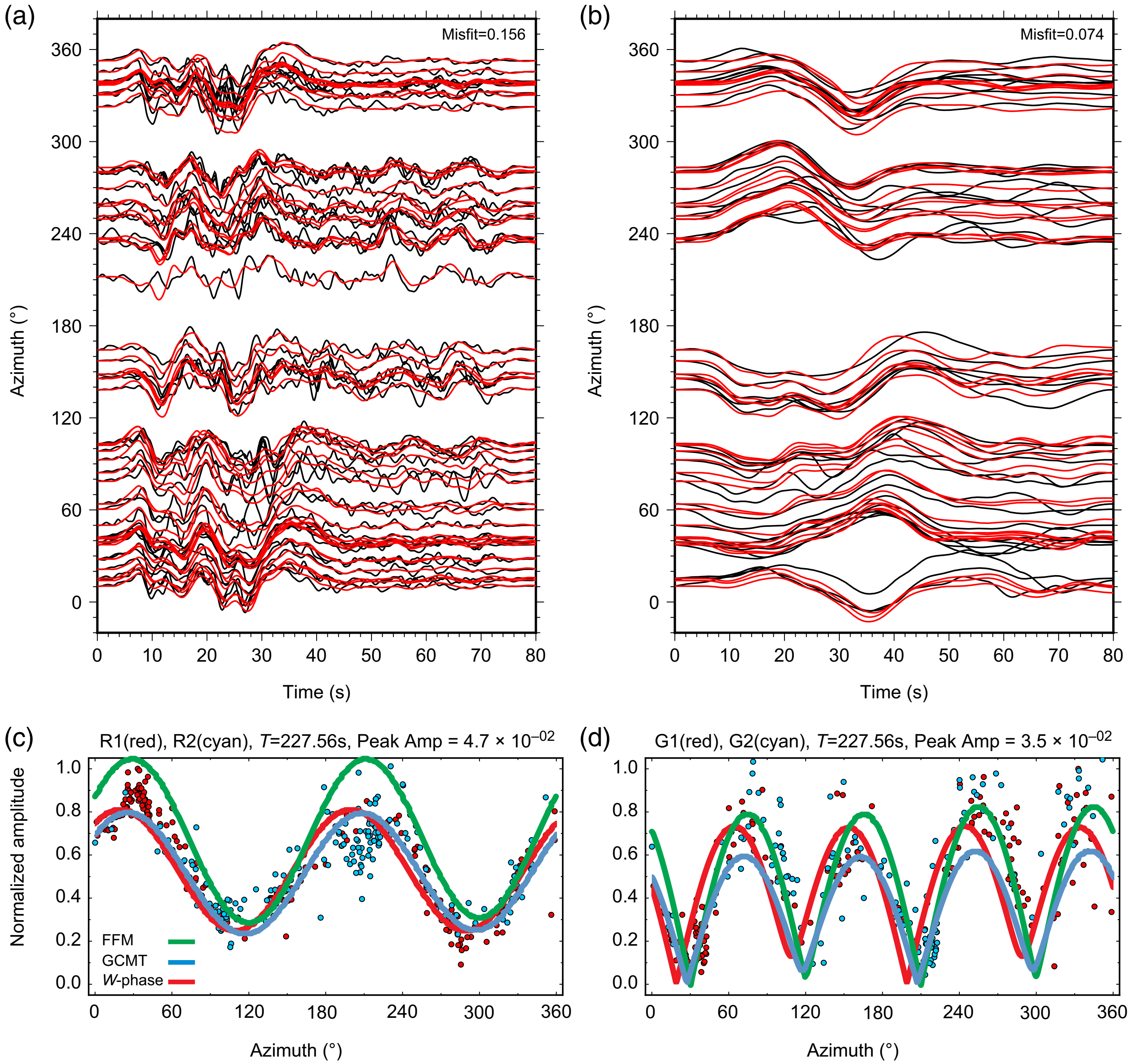

long-period spectral amplitudes comparably or better than the long-period moment tensor inversions, confirming that the seismic moment and finite-fault model geometry are consistent with the long-period data. The seismic moment of the three-segment model is intermediate between those of the *W*-phase and Global CMT solutions, but the long-period surface-wave excitation is stronger for the finite-fault model with half of the moment on segments having greater dip (30°–37°).

The finite-fault model was also used to compute the tsunami signals using publicly available bathymetry information

Figure 4. (a,b) Comparisons of observed (black lines) and predicted (red lines) teleseismic *P* and *SH* waves, respectively. The waveform misfit values are shown at top right. (c,d) The observed and predicted Rayleigh- and Love-wave source spectral amplitudes for period T = 227.56 s, respectively. Red dots indicate short-arc (R1, G1) observations, and cyan dots indicate long-arc (R2, G2) observations. Theoretical spectral amplitudes for the point-source moment tensors of the USGS-NEIC *W*-phase, Global CMT, and our three-fault segment model are shown by red, light blue, and green curves, respectively.

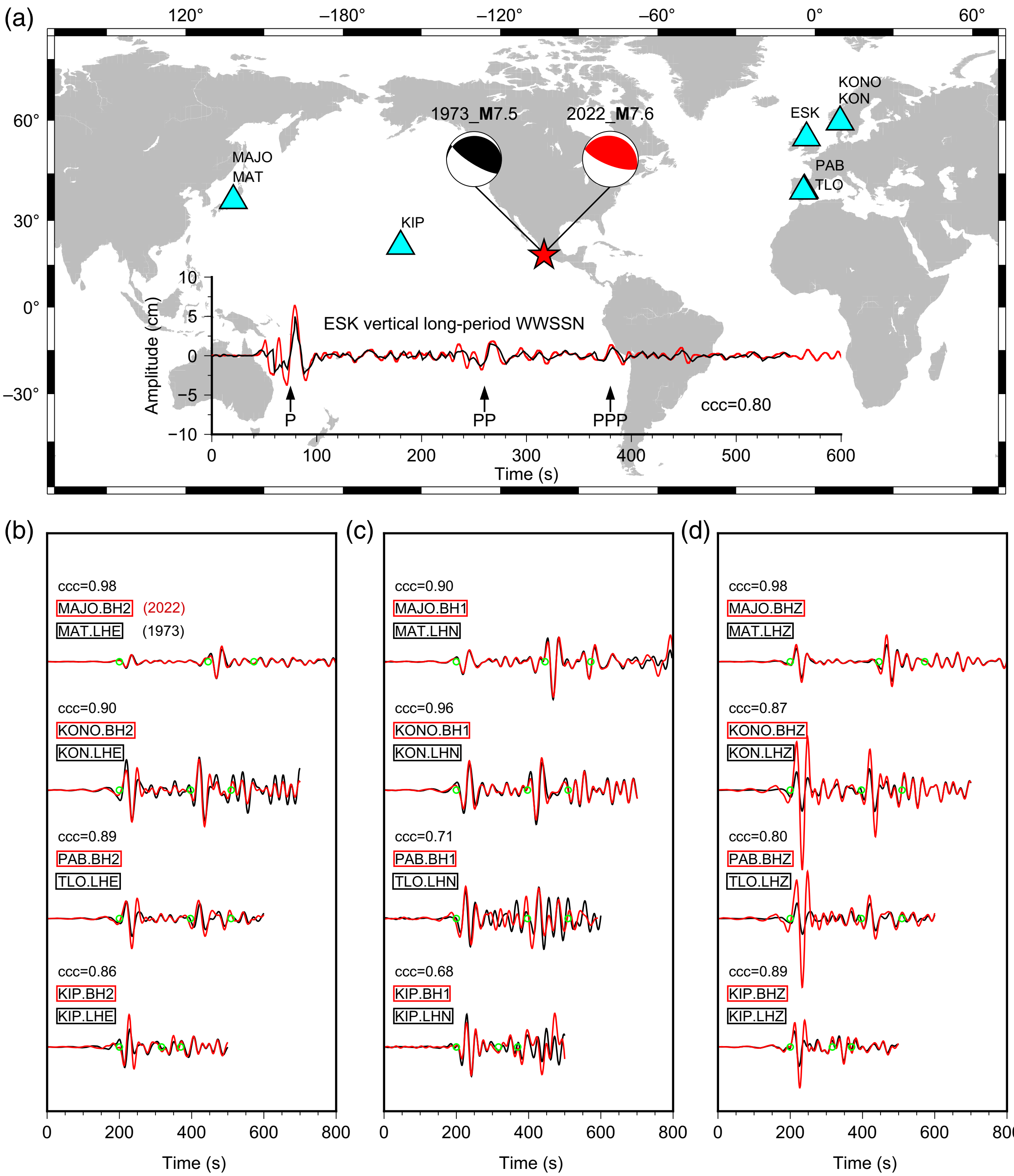

Figure 5. Teleseismic waveform comparisons between the 2022 (red) and 1973 (black) events. (a) The cyan triangles show the locations of the stations used for comparisons. The red and black focal mechanisms are the best double-couple solutions for the 2022 and 1973 (Chael and Stewart, 1982) events. The lower inset shows the vertical *P*-wave comparisons between the 2022 (red) and 1973 (black) events at World Wide Standard Seismograph Network station ESK. (b–d) Three-component digitally recorded waveforms of 2022 (red) and 1973 (black) earthquakes filtered in the frequency band of 0.015–0.05 Hz. Green circles mark the sequential arrivals of *P*, *PP*, *PPP*, and *S* waves. For the 2022 event, BH1 is north–south, and BH2 is east–west for all the cases.

and the tsunami modeling code NEOWAVE (Yamazaki *et al.*, 2009; Bai *et al.*, 2018). Based on the one-layer nonhydrostatic free-surface flow theory (Bai and Cheung, 2013), the NEOWAVE model can resolve the linear profile of the vertical velocity through the pressure Poisson equation for weakly dispersive tsunami waves. The code is built upon a staggered finite-difference scheme for numerical stability and equipped with a shock-capturing scheme to approximate wave breaking. The kinematic seafloor boundary condition can effectively capture the evolution of seafloor displacement induced by the finite-fault model and transmit the energy to sea surface in real time to fully reconstruct the time history of tsunami generation. A computational grid with 15 arcsec resolution (Fig. 3a) is used to resolve key bathymetric features relevant to the nearshore tide gauges and deep-sea DART station.

The tsunami results generated by the finite-fault model are compared with the observational records at DART 43412 and five tide gauges in Figure 3b. The arrival time and the amplitude of the first peak produced by the model reasonably match with the observation at DART 43412, indicating a viable distribution of slip along the dip direction of the finite-fault model relative to the coastline and the trench. Although the arrival of the tsunami is obscured by short-period signals in the measurements of the Puerto Vallarta tide gauge, the 50 min long-period oscillation with less than 5 cm amplitude is reproduced by the tsunami model. The Manzanillo tide gauge is situated at an inner harbor connected with Manzanillo Bay through a channel. The model output locates close to the gauge but in the bay due to low resolution of the bathymetry, which limits how well the data can be matched. Despite the differences in amplitude, the observed and computed tsunami signals oscillate in a relatively phase-locked way for at least five periods, implying that the tsunami response in the bay is basically recovered. The port Lazaro tide gauge is surrounded by intricate waterways and estuaries, so the tsunami model with low-resolution bathymetry is not able to match details. However, a persistent undulation with approximately 20 min peak period from the model can still be validated by the measurement, because both the time series start to synchronize from 2.5 to 4.5 hr after the first couple of tsunami surges. The initial oscillations in the Zihuatanejo tide gauge record are well predicted by the tsunami model, and later misfits are probably due to the limited representation of the bay area by the current computational grid. The waveform at Acapulco is generally matched by the tsunami model despite amplitude underestimation for a couple of cycles, and the enduring 30 min period surges indicate that the tsunami triggered coastal resonance in Acapulco Bay.

Discussion and Conclusions

The finite-fault model obtained here can be compared with the USGS-NEIC finite-fault model produced using a newly introduced (Goldberg *et al.*, 2022) procedure of joint inversion of teleseismic body and surface waves, GNSS static and high-rate waveforms, and InSAR observations (see Data and Resources), which largely parallels the application we have followed. The USGS-NEIC planar model ($\phi = 295°$, $\delta = 22°$) uses the SSN hypocenter and has an elongated large-slip patch extending northwest of the hypocenter, with $M_0 = 2.73 \times 10^{20}$ N · m (M_w 7.6) and peak slip of ~3.2 m, and a moment rate function very similar in shape to our preferred model. The secondary differences between the solutions may be caused by choices of smoothing and size of the subfaults in the model representations, but we also use a deeper hypocenter and depth-varying dip model, which conform to the shallow Slab2 interface geometry (Fig. 2a). We also perform independent tsunami forward modeling (Fig. 3), which supports the overall model validity. The consistency between the different inversions is very encouraging and justifies further assessment of the rupture model. It also indicates that the routine procedures now being upgraded by the USGS-NEIC are attaining more reliable finite-fault solutions than has been found for the earlier solutions using only teleseismic data (Goldberg *et al.*, 2022).

It is commonly observed that aftershocks for large subduction zone earthquakes are relatively sparse within areas of large coseismic slip and mainly distributed around their margins (Wetzler *et al.*, 2018). We superimposed the first two months of aftershocks ($M \geq 4.0$) of the 2022 Michoacán earthquake on our preferred slip model (Fig. 2a). Most aftershocks are located in the up-dip portion of the rupture zone, and only a few are located in the large-slip region. There is a concentration of aftershocks near the southeast edge of the rupture, including events with $M \geq 5$, suggesting a stress concentration on that end of the mainshock rupture. To the northwest, the slip propagation of the 2022 event terminated at the edge of the 2003 rupture zone, indicating that the stress is not concentrated enough to result in continued rupture.

The rupture zone of the 2022 event overlaps the source region of the 1973 M_w 7.6 earthquake outlined by aftershocks (Reyes *et al.*, 1979; Ruff and Miller, 1994) and a limited resolution finite-fault model (Santoyo *et al.*, 2006), but it is hard to evaluate the similarity of the events from these measurements. Repeating earthquakes are characterized by having highly correlated seismic waveforms and are often interpreted as reflecting repeated rupture of persistent asperities (Ye *et al.*, 2016). Thus, to further compare the events, we consider teleseismic waveforms recorded for the 1973 and 2022 events at five seismic stations ESK, KIP, KON/KONO, MAT/MAJO, and TLO/PAB, respectively (Fig. 5). The long-period vertical component recording at ESK for the 1973 event is from a World Wide Standard Seismograph Network (WWSSN) station, spanning multiple *P* waves (*P*, *PP*, and *PPP*; Chael and Stewart, 1982). Short segments of the long-period *P* waves for additional WWSSN stations for the 1973 event are shown in Chael and Stewart (1982), and these can be compared with the 2022 signals at the same or nearby stations; however, it is more beneficial to compare longer three-component recordings spanning the direct *P*and *S* body-wave arrivals. This has not previously been possible for repeated large ruptures around the circum Pacific, because the earlier events have predated digital recordings, and long segments of WWSSN signals, including *S* waves, are commonly off-scale or very difficult to digitize. Fortunately, the 1973 event was recorded by several early digital three-component seismic stations in the 50°–110° angular distance range (KIP, KON, MAT, and TLO) from the high-gain long-period (HGLP) network (Fig. 5b–d). The HGLP seismometer was a narrow band with peak gain at ∼50 s, so only longer period signals can be compared. Waveforms for the 2022 event are from GSN broadband stations colocated or very close to the WWSSN and HGLP stations.

For direct comparison, the broadband waveform at ESK for the 2022 event is transferred to a WWSSN long-period response. The *P*, *PP*, and*PPP* phases are visually similar, with comparable overall duration and initial double-pulse complexity of the direct *P* phase (Fig. 5a). The *P* wave of the 1973 event at ESK is more complex than for comparable magnitude events along the Mexican subduction zone (Chael and Stewart, 1982; Astiz *et al.*, 1987), which are typically associated with single strong impulses associated with large discrete asperities. Allowing for errors in digitizing WWSSN paper records or film chips and uncertainties in precise ESK instrument response, the ESK waveform comparison of the normalized cross-correlation coefficient of 0.8 for the full waveform indicates a pronounced similarity of the 1973 and 2022 ruptures (Fig. 5a), and this holds for the other *P*-wave recordings displayed by Chael and Stewart (1982). Comparing the ground displacement waveforms for HGLP and GSN stations in the frequency band 0.015–0.05 Hz reveals that the *P* and *PP* waveforms are also very similar, with correlation coefficients ranging from 0.68 to 0.98, although the 2022 event produced larger amplitude vertical component signals at most stations (Fig. 5d). Based on these intermediate period comparisons, we characterize the 2022 event as a quasi-repeat of the 1973 event, with similar overall rupture durations and degree of asperity complexity, indicating persistence of the patchy coupling distribution. This finding suggests that comparisons of complete three-component records can detect rupture differences that are not evident in just vertical component *P* waveform comparisons. Because we can expect more large-event recurrences for which increasingly extensive digital seismic recordings will be available for the earlier events, more quantitative comparison of signals and slip models to assess asperity persistence and dynamic rupture similarity will become possible.

Data and Resources

Three-component records of the 2022 and 1973 earthquakes were obtained from the Incorporated Research Institutions for Seismology (IRIS) data center (http://ds.iris.edu/wilber3/find_event). Raw high-rate GNSS data are available at the GAGE Facility archive, operated by UNAVCO (https://data.unavco.org/archive/gnss/highrate/1-Hz/rinex/2022/262/). The UNAVCO Bulletin Board provided coseismic GNSS statics at https://data.unavco.org/archive/gnss/products/event/. The Sentinel-1 synthetic aperture radar (SAR) data were retrieved and downloaded from the Alaska Satellite Facility Distributed Active Archive Center (ASF DAAC; https://vertex.daac.asf.alaska.edu/). The Global Centroid Moment Tensor (Global CMT) solution is available at https://www.globalcmt.org/CMTsearch.html. The finite-slip model is from https://earthquake.usgs.gov/earthquakes/eventpage/us7000i9bw/finite-fault. Broadband radiated elastic energy in the far field is from IRIS EQEnergy (DOI: 10.17611/DP/EQE.1). U.S. Geological Survey National Earthquake Information Center (USGS-NEIC) information is available at https://www.usgs.gov/programs/earthquake-hazards/earthquakes. The raw tide gauge records were downloaded from the Intergovernmental Oceanographic Commission (IOC) at. The tsunami records from the Deep-Ocean Assessment and Reporting of Tsunamis (DART) network were obtained from the National Oceanic and Atmospheric Administration (NOAA) National Data Buoy Center (http://www.ndbc.noaa.gov). Topography and bathymetry are from SRTM15_PLUS (ftp://topex.ucsd.edu/pub/srtm15_plus/). Aftershocks are from Servicio Sismológico Nacional (SSN) catalog (http://www2.ssn.unam.mx:8080/catalogo/). Rupture areas of subduction earthquakes in Mexico are digitized from http://usuarios.geofisica.unam.mx/vladimir/images/EQ_map_2013_es_clear.jpg. All websites were last accessed in March 2023.

Declaration of Competing Interests

The authors acknowledge that there are no conflicts of interest recorded.

Acknowledgments

The authors thank the two anonymous reviewers for their helpful comments on this article. The authors thank the facilities of Incorporated Research Institutions for Seismology (IRIS) Data Services, and specifically the IRIS Data Management Center, which were used for access to teleseismic waveforms, related metadata, and/or derived products used in this study. The authors thank the European Space Agency for the Sentinel-1 data, and UNAVCO for the coseismic GNSS statics and high-rate GNSS waveforms. The authors also thank the Canadian Spatial Reference System precise point positioning (CSRS-PPP) online service system for high-rate GNSS data processing (https://webapp.geod.nrcan.gc.ca/geod/tools-outils/ppp.php, last accessed March 2023). Chengli Liu was supported by the National Science Foundation of China (Number 42222403). Thorne Lay's earthquake research is supported by the U.S. National Science Foundation grant EAR1802364. Yefei Bai's tsunami research is supported by Finance Science and Technology Project of Hainan Province (Number ZDKJ202019).

References

Abbott, E. R., and M. R. Brudzinski (2015). Shallow seismicity patterns in the northwestern section of the Mexico subduction zone, *J. South Am. Earth Sci.* **63,** 279–292.

Astiz, L., H. Kanamori, and H. Eissler (1987). Source characteristics of earthquakes in the Michoacán seismic gap in Mexico, *Bull. Seismol. Soc. Am.* **77,** 1326–1346.

Bai, Y., and K. F. Cheung (2013). Dispersion and nonlinearity of multi-layer non-hydrostatic free-surface flow, *J. Fluid Mech.* **726,** 226–260.

Bai, Y., Y. Yamazaki, and K. F. Cheung (2018). Convergence of multilayer non-hydrostatic models in relation to Boussinesq-type equations, *J. Waterw. Port Coastal Ocean Eng.* **144,** no. 2, 06018001 .

Brudzinski, M. R., K. M. Schlanser, N. J. Kelly, C. DeMets, S. P. Grand, B. Márquez-Azúa, and E. Cabral-Cano (2016). Tectonic tremor and slow slip along the northwestern section of the Mexico subduction zone, *Earth Planet. Sci. Lett.* **454,** 259–271.

Chael, E. P., and G. S. Stewart (1982). Recent large earthquakes along the Middle American trench and their implications for the subduction process, *J. Geophys. Res.* **87,** no. B1, 329–338.

Convers, J. A., and A. V. Newman (2011). Global evaluation of large earthquake energy from 1997 through mid-2010, *J. Geophys. Res.* **116,** B08304 , 1–17.

Cosenza-Muralles, B., C. DeMets, B. Márques-Azúa, O. Sánchez, J. Stock, E. Cabral-Cano, and R. McCafrey (2022). GPS-derived interseismic locking along the Jalisco-Colima segment of the Mexico subduction zone, *Geophys. J. Int.* **228,** 2174–2197.

Cruz-Atienza, V. M., J. Tago, C. Villafuerte, M. Wei, R. Garza-Girón, L. A. Dominguez, V. Kostoglodov, T. Nishimura, S. I. Franco, J. Real, *et al.* (2021). Short-term interaction between silent and devastating earthquakes in Mexico, *Nat. Commun.* **12,** no. 1, 1–14.

DeMets, C., R. G. Gordon, and D. F. Argus (2010). Geologically current plate motions, *Geophys. J. Int.* **181,** no. 1, 1–80.

Dominguez, L. A., T. A. Taira, V. M. Cruz-Atienza, A. Iglesias, C. Villafuerte, D. Legrand, X. Pérez-Campos, and M. Raggi (2022). Interplate slip rate variation between closely spaced earthquakes in southern Mexico: The 2012 Ometepec and 2018 Pinotepa Nacional thrust events. *J. Geophys. Res. Solid Earth*, e2022JB024292.

Farr, T. G., P. A. Rosen, E. Caro, R. Crippen, R. Duren, S. Hensley, M. Kobrick, M. Paller, E. Rodriguez, L. Roth, *et al.* (2007). The shuttle radar topography mission, *Rev. Geophys.* **45,** no. 2, RG2004.

Franco, S. I., V. Kostoglodov, K. M. Larson, V. C. Manea, M. Manea, and J. A. Santiago (2005). Propagation of the 2001–2002 silent earthquake and interplate coupling in the Oaxaca subduction zone, Mexico, *Earth Planets Space* **57,** no. 10, 973–985.

Goldberg, D. E., P. Koch, D. Melgar, S. Riquelme, and W. L. Yeck (2022). Beyond the teleseism: Introducing regional seismic and geodetic data into routine USGS finite-fault modeling, *Seismol. Res. Lett.* **93,** no. 6, 3308–3323.

Gómez-González, J. M., C. Mendoza, A. Sladen, and M. Guzmán-Speziale (2010). Kinematic source analysis of the 2003 Tecomán, México, earthquake (Mw 7.6) using teleseismic body waves. *Boletín de la Soc. Geol. Mex.* **62,** no. 2, 249–262.

Graham, S. E., C. DeMets, E. Cabral-Cano, V. Kostoglodov, A. Walpersdorf, N. Cotte, M. Brudzinski, R. McCaffrey, and L. Salazar-Tlaczani (2014). GPS constraints on the 2011–2012 Oaxaca slow slip event that preceded the 2012 March 20 Ometepec earthquake, southern Mexico, *Geophys. J. Int.* **197,** no. 3, 1593–1607.

Hayes, G. P., G. L. Moore, D. E. Portner, M. Hearne, H. Flamme, M. Furtney, and G. M. Smoczyk (2018). Slab2, a comprehensive subduction zone geometry model, *Science* **362,** no. 6410, 58–61.

Iglesias, A., S. K. Singh, O. Castro-Artola, X. Pérez-Campos, R. D. Corona-Fernandez, M. A. Santoyo, V. H. Espíndola, D. Arroyo, and S. I. Franco (2022). A source study of the MW 7.0 Acapulco, Mexico, earthquake of 8 September 2021, *Seismol. Res. Lett.* **93,** no. 6, 3205–3218.

Ji, C., D. J. Wald, and D. V. Helmberger (2002). Source description of the 1999 Hector Mine, California, earthquake, part I: Wavelet domain inversion theory and resolution analysis, *Bull. Seismol. Soc. Am.* **92,** no. 4, 1192–1207.

Ji, C., D. V. Helmberger, D. J. Wald, and K. F. Ma (2003). Slip history and dynamic implications of the 1999 Chi-Chi, Taiwan, earthquake, *J. Geophys. Res.* **108,** no. B9, 2412.

Kanamori, H., and J. W. Given (1981). Use of long-period surface waves for rapid determination of earthquake-source parameters, *Phys. Earth Planet. Inter.* **27,** no. 1, 8–31.

Liu, C., T. Lay, Z. Xie, and X. Xiong (2019). Intraslab deformation in the 30 November 2018 Anchorage, Alaska, M_W 7.1 earthquake, *Geophys. Res. Lett.* **46,** no. 5, 2449–2457.

Martínez López, M. R., and C. Mendoza (2018). Caracterización de asperezas de sismos receientes en la zona de subducción de Michoacán-Colima-Jalisco, México, *Geofísica Internacional* **57,** no. 4, 289–306 (in Spanish).

Mendoza, C., and S. H. Hartzell (1989). Slip distribution o the 19 September 1985 Michoacán, Mexico, earthquake: Near-source and teleseismic constraints, *Bull. Seismol. Soc. Am.* **79,** no. 3, 665–669.

Mendoza, C., and S. H. Hartzell (1997). Fault slip distribution of the 1995 Colima-Jalisco, Mexico, earthquake, *Bull. Seismol. Soc. Am.* **89,** 1338–1344.

Ortiz, M., S. K. Singh, J. Pacheco, and V. Kostoglodov (1998). Rupture length of the October 9, 1995 Colima-Jalisco earthquake (M_W 8) estimated from tsunami data, *Geophys. Res. Lett.* **25,** no. 15, 2857–2860.

Ramírez-Herrera, M. T., V. Kostoglodov, and J. Urrutia-Fucugauchi (2010). Overview of recent coastal tectonic deformation in the Mexican subduction zone, *Pure Appl. Geophys.* **168,** no. 8, 1425–1433.

Reyes, A., J. N. Brune, and C. Lomnitz (1979). Source mechanism and aftershock study of the Colima, Mexico earthquake of January 30, 1973, *Bull. Seismol. Soc. Am.* **69,** no. 6, 1819–1840.

Ruff, L. J., and A. D. Miller (1994). Rupture process of large earthquakes in the northern Mexico subduction zone, *Pure Appl. Geophys.* **142,** no. 1, 101–172.

Santoyo, M. A., T. Mikumo, and L. Quintanar (2006). Faulting process and coseismic stress change during the 30 January, 1973, Colima, Mexico interplate earthquake (MW=7.6), *Geofís. Int.* **45,** no. 3, 163–178.

Singh, S. K., and F. Mortera (1991). Source time functions of large Mexican subduction earthquakes, morphology of the Benioff zone, age of the plate, and their tectonic implications, *J. Geophys. Res.* **96,** no. B13, 21,487–21,502.

Singh, S. K., L. Astiz, and J. Havskov (1981). Seismic gaps and recurrence periods of large earthquakes along the Mexican subduction zone: A reexamination, *Bull. Seismol. Soc. Am.* **71,** 827–843.

Singh, S. K., L. Ponce, and S. P. Nishenko (1985). The great Jalisco, Mexico, earthquakes of 1932: Subduction of the Rivera plate, *Bull. Seismol. Soc. Am.* **75,** no. 5, 1301–1313.

UNAM Seismology Group (1986). The September 1985 Michoacán earthquakes: Aftershock distribution and history of rupture, *Geophys. Res. Lett.* **13,** no. 6, 573–576.

Wegnüller, U., C. Werner, T. Strozzi, A. Wiesmann, O. Frey, and M. Santoro (2016). Sentinel-1 support in the GAMMA software, *Procedia Comput. Sci.* **100,** 1305–1312.

Wetzler, N., T. Lay, E. E. Brodsky, and H. Kanamori (2018). Systematic deficiency of aftershocks in areas of high coseismic slip for large subduction zone earthquakes, *Sci. Adv.* **4,** no. 2, eaao3225 .

Yagi, Y., T. Mikumo, J. Pacheco, and G. Reyes (2004). Source rupture process of the Tecomán, Colima, Mexico earthquake of 22 January 2003, determined by joint inversion of teleseismic body-wave and near-source data, *Bull. Seismol. Soc. Am.* **94,** no. 5, 1795–1807.

Yamazaki, Y., Z. Kowalik, and K. F. Cheung (2009). Depth-integrated, non-hydrostatic model for wave breaking and run-up, *Int. J. Numer. Methods Fluids* **61,** no. 5, 473–497.

Yan, Z., X. Xiong, C. Liu, and J. Xu (2022). Integrated Analysis of the 2020 Mw 7.4 La Crucecita, Oaxaca, Mexico, earthquake from joint inversion of geodetic and seismic observations, *Bull. Seismol. Soc. Am.* **112,** no. 3, 1271–1283.

Ye, L., H. Kanamori, J. P. Avouac, L. Li, K. F. Cheung, and T. Lay (2016). The 16 April 2016, M_W 7.8 (MS 7.5) Ecuador earthquake: A quasi-repeat of the 1942 M_S 7.5 earthquake and partial re-rupture of the 1906 M_S 8.6 Colombia–Ecuador earthquake, *Earth Planet. Sci. Lett.* **454,** 248–258.

Manuscript received 5 December 2022
Published online 3 April 2023